Simultaneous angular rate estimates extracted from a single axisymmetric resonator

Howard H. Ge, Robert M'Closkey†
Mechanical and Aerospace Engineering
Samueli School of Engineering and Applied Science
University of California, Los Angeles, CA 90095

***Abstract*—An axisymmetric planar MEMS resonator is configured such that the $n = 2$ elliptical pair of modes near 13.5 kHz, and the $n = 3$ pair of modes near 23.8 kHz, are both degenerate, that is, the frequency difference within a given pair of modes is close to the resonance bandwidth. This configuration enables not only the exploitation of the standard elliptical pair of modes for angular rate sensing but also permits the operation of the $n = 3$ pair of modes as a high-sensitivity Coriolis vibratory gyro. The performance for each pair of modes separately acting as a vibratory gyro is quantified, however, the control architecture also facilitates the *simultaneous* operation of both pairs of modes. In this scenario, two measurements of angular rate are extracted from a single resonator and although the short-term rate noise associated with the $n = 3$ pair is an order of magnitude larger than the rate extracted from the $n = 2$ pair, the long-term drift in the rate offsets are correlated. Thus, a filter architecture for fusing the rate measurements is proposed and it is shown how the derived rate estimate possesses superior offset stability but also retains the low short-term noise associated with the rate measurement from the $n = 2$ pair.**

***Index Terms*—Gyroscopes, MEMS, inertial sensors, bias self calibration**

I. Introduction

Coriolis vibratory gyros created with planar MEM resonators have demonstrated high signal-to-noise ratios, especially in frequency-matched configurations. Planar frequency-matched designs in which two modes possess nominally degenerate natural frequencies are reported in [1–5]. The frequency-matching boosts the SNR with respect to buffer noise, however, the sensitivity of the zero rate bias (rate offset) to subtle changes in the resonator dynamics, especially changes in damping, is still a major issue. Anything that changes the effective damping in the modes will create drift in the rate offset and so compensating or reducing the offset drift is of paramount importance in these sensors if the benefits of the high SNR are to be fully realized. Thermal control and isolation of the resonator is always employed when practical because many sources of resonator damping perturbations, whether induced by stresses or temperature dependence of the dissipation of the resonator material, can ultimately be traced to the temperature stability of the resonator and its package. These techniques, though not reviewed here, are based on creating a stable environment for the resonator and are often used with the offset *compensation* approaches discussed below.

†Corresponding author, rtm@seas.ucla.edu. This work was partially supported by DARPA contract W31P4Q-11-1-0004.

A complimentary set of techniques have been developed to compensate for drift in the rate offset of MEM gyros. These techniques can be roughly categorized as *extrinsic* or *intrinsic*. Extrinsic techniques employ additional hardware to provide known stimuli to the gyro for calibration purposes. These techniques can be very effective, but come with the added complexity of mechanical design, integration and packaging. For example, a rotary platform was used in [6] to AC-couple low frequency rate inputs so that the offset can be effectively removed by filtering. Intrinsic approaches don't rely on additional external stimuli but instead compensate the offset drift by identifying additional measurements that are correlated with the drift, eg. embedded strain gauges fabricated with the resonator as recently reported in [7], or operating the resonator in such a manner that certain errors are reduced by averaging, eg. the periodic "mode switching" reported in [4, 8] for disk resonators and in [9] for hemispherical resonators, or the modal precession technique described in [10].

The resonators in the aforementioned references which are ring/disk-type resonators all exploit the $n = 2$ pair of modes for angular rate sensing. The terminology comes from the fact that the mode shapes are dominated by 2θ dependency on the sensor-fixed angular coordinate θ. It is well-known that other pairs of nominally degenerate modes in ring resonators are also coupled by Coriolis terms in the sensor-fixed coordinate system and, thus, can also be used for angular rate sensing [11]. Although diminishing returns are obtained with the use of higher-order pairs due to their reduced degree of Coriolis coupling compared to the $n = 2$ pair, one contribution of this paper is to provide a definitive comparison between the frequency-matched operation of the $n = 3$ pair to the operation of the $n = 2$ pair for the resonator described in [12]. The frequency matching in this reference was accomplished by applying mass-deposition techniques but only considered the $n = 2$ pair. In the present paper the $n = 3$ pair of modes is targeted as well and we show that the square root of the power spectral density of the noise associated with the $n = 3$-derived angular rate is about an order of magnitude greater than the root-density associated with the $n = 2$-derived rate. This large difference is primarily due to the relative response amplitudes that can be developed within each pair using comparable amplitudes of electrostatic forcing –in other words, the weaker Coriolis coupling of the $n = 3$ pair is not the dominant factor for the resonator under consideration in this paper. The lower response amplitudes of

the $n = 3$ pair are a consequence of their higher intrinsic stiffnesses and lower time constants. Thus, as far as silicon resonator considered in this paper is concerned, the $n = 2$ pair will always achieve a higher SNR than the $n = 3$ pair under similar forcing conditions, electrode areas and so forth. Resonators fabricated from other materials may not suffer from this limitation since thermoelastic dissipation models of fused silica rings, for example, suggest similar time constants for both $n = 2, 3$ pairs when certain ring dimensions are used, eg. the results in [13] can be adapted for fused silica rings.

The modal degeneracy of the $n = 2$ pair and the modal degeneracy of the $n = 3$ pair are actually achieved within the same resonator. Thus, the second contribution of the paper demonstrates that both pairs of modes can be *simultaneously* operated as high SNR Coriolis vibratory gyros. Thus, one resonator yields two angular rate measurements. It is shown that this "dual-pair" operation only slightly degrades the rate noise spectra compared to single-pair operation. Finally, the dual-pair operation also reveals strong correlation between the two rate offsets. Perhaps this is not surprising considering that what drives the offset drift in one pair will also have some effect on the other pair. The coupling of the offsets means appropriate filtering can be used to mitigate their drift. Thus, the third contribution of the paper is a proposed filter structure that fuses the two rate signals into a single rate estimate with reduced offset drift. This alternative approach for compensating long-term instability can be used in conjunction with any of the other aforementioned techniques.

The paper is organized as follows. Sec. II describes the resonator-level configuration of the electrodes in order to support dual-pair operation. Sec. III describes the controller architecture that enables both single- and dual-pair CVG operation. Sec. IV presents experimental results for both $n = 2, 3$ single-pair operation as well as their simultaneous operation. Sec. V proposes a filtering scheme whereby the rate measurements from the dual-pair operation are fused into a single estimate of angular rate with improved offset stability. Sec. VI concludes the paper.

II. Resonator Configuration

The resonator under consideration is described in [12]. The reader is referred to this paper for details on its fabrication, testing and modeling but, broadly speaking, the resonator can be viewed as a ring in which modes corresponding to eigenfunctions $\cos(n\theta)$ and $\sin(n\theta)$, $n = 2, 3, \ldots$, appear in degenerate pairs, where θ parameterizes the position on the ring according to an angle coordinate. In physical devices, though, there is some detuning of the resonant frequencies in any given pair. Since the electronic buffer noise dominates the pick-off noise spectrum for this design, detuning can severely degrade the gyro performance [14]. Thus, reducing the frequency mismatch within the $n = 2$ pair of modes and, simultaneously, within the $n = 3$ pair of modes is necessary for maximizing the signal-to-noise ratio of the angular rate measurements extracted from each pair. Furthermore, reducing the frequency mismatch also reduces the quadrature offset, which is desirable since it avoids saturation of the high-gain force-to-rebalance (FTR) loop and also minimizes coupling into the rate offset when there are demodulation phase errors.

TABLE I
Summary of Modal Properties

Pair	Nominal ω_n (kHz)	Difference (Hz)	Quality Factor (k)
$n = 2$	13.517	0.12	50.6/50.6
$n = 3$	23.753	0.10	35.5/35.8

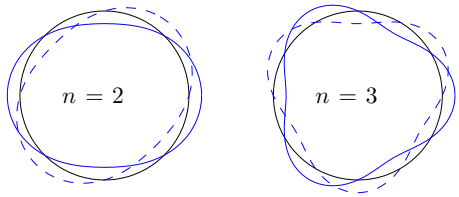

The $n = 2$ frequency mismatch can be reduced to about 50 mHz (out of a nominal modal frequency of approximately 13.5 kHz) via point-mass loading of the resonator as demonstrated in [12], however, the effect of mass loading on the $n = 3$ frequency mismatch was ignored. It is necessary to simultaneously reduce the mismatch if low noise measurements of angular rate are desired from each pair of modes within the same resonator. Thus, the mass loading technique was extended to reduce within the same resonator the $n = 3$ frequency mismatch in addition to the $n = 2$ mismatch [15]. The added complexity of reducing the mismatch in both pairs of modes, though, means that it is typically not possible to achieve the same level of mismatch reduction as in the cases where the $n = 2$ pair or $n = 3$ pair are separately considered because the mass loading technique discussed in these references deposits quantized amounts of mass on to the resonator, i.e. arbitrarily fine increments are not possible. Recent work in [16] proposes mass removal via etching of selected sites may mitigate this constraint, however, this technique has not been applied to the dual pair tuning problem. The resonator reported in [15] is used for the present work and so only the final frequency mismatches and quality factors are reported in Table I. The approximate mode shapes when $n = 2, 3$ are also shown.

The antinodes associated with the $n = 2$ mode shapes subtend 45 degrees, and the antinodes associated with the $n = 3$ mode shapes subtend 30 degrees, so the electrode arrangement is selected to optimally sense and excite these pairs by selecting the forcer and pick-off electrodes to subtend the same angles, however, since there is some freedom in assigning the electrodes even with these constraints, the final layout is chosen to minimize quadrature and capacitive feedthrough. The electrode configuration, shown in Fig. 1, is different from the configuration reported in [15]. The D_1 and D_2 electrodes are for forcing the $n = 2$ modes, and the S_1 and S_2 electrodes are the $n = 2$ pick-offs. Similarly, the D_3^+, D_3^-, D_4^+ and D_4^- electrodes are for forcing the $n = 3$ modes and the S_3^+, S_3^- and S_4 are the $n = 3$ pick-offs. The forcing electrodes for the $n = 3$ modes are arranged as two differential pairs, however, only the S_3 pick-off is differential (S_3 is the force-to-rebalance pick-off –see Sec. III). It is desirable to

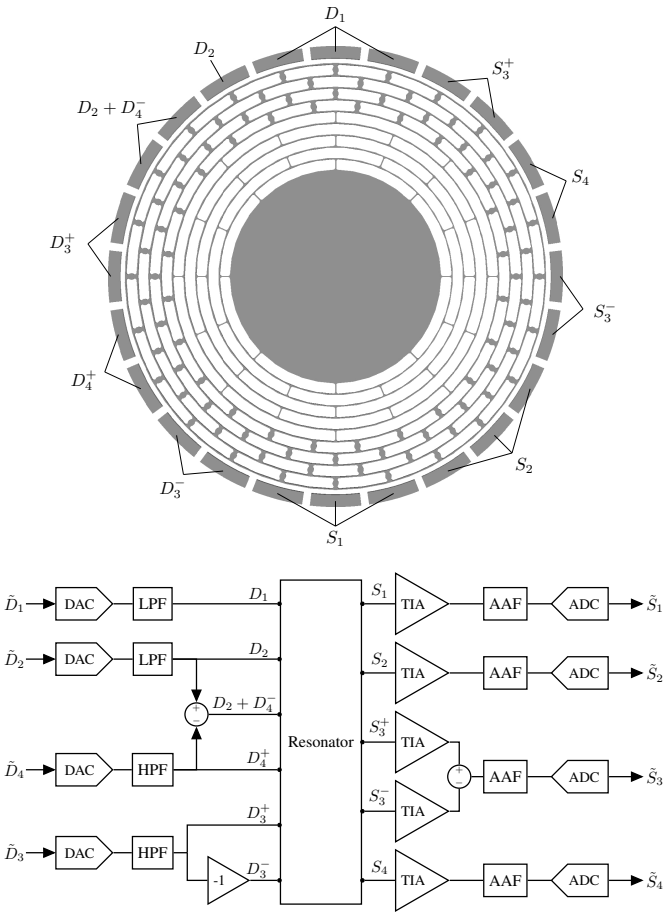

Fig. 1. (top) Electrode layout on resonator. (Bottom) Functional block diagram showing relationship between discrete-time signals and electrode signals.

arrange all electrodes/forcers into differential pairs to mitigate capacitive coupling between electrodes, however, due to the limited number of electrodes, differential sensing is allocated to the paths where the coupling is most detrimental.

All pickoff electrode currents are buffered by transresistance amplifiers with 10 MΩ feedback resistors. Since the resonator is unpackaged, the buffer card is co-located with the resonator in a vacuum chamber and all other electronics are located outside the chamber. A digital signal processor (DSP) executing at an 80 kHz sample rate interfaces to 16-bit analog-to-digital convertors (ADCs) and digital-to-analog convertors (DACs). The buffer card outputs are filtered by anti-alias filters prior to sampling. The anti-alias filters are denoted by the "AAF" blocks in Fig. 1. The block diagram also shows how the electrode signals are consolidated and sampled. The discrete-time signals manipulated by the DSP are given the ˜ notation. The automatic gain control (AGC) forcing signals issued by the DSP are denoted $\tilde{D}_1$ and $\tilde{D}_3$ for the $n = 2$ and $n = 3$ pairs, respectively. The FTR forcing signals are denoted $\tilde{D}_2$ and $\tilde{D}_4$ for the $n = 2$ and $n = 3$ pairs, respectively. The signals $\tilde{S}_1$ and $\tilde{S}_3$ are the AGC pick-offs, and $\tilde{S}_2$ and $\tilde{S}_4$ are the force-to-rebalance pick-offs. The frequency responses from the perspective of the DSP for all 16 channels are shown in Figs. 2 and 3 in a neighborhood of each

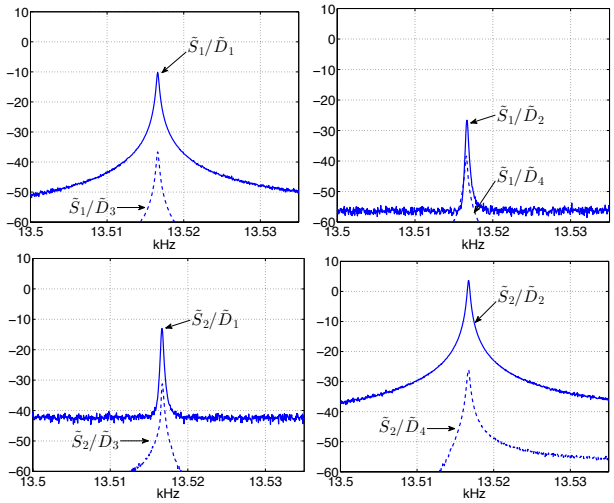

Fig. 2. Frequency responses for electrode arrangement shown in Fig. 1. The solid traces are used for designing the control filters for the $n = 2$ pair, however, the dashed traces show how the forcers for the $n = 3$ pair couple into the $n = 2$ pair.

modal pair. The frequency response magnitude of all channels is shown to reveal the coupling that exists between the forcing electrodes to both pairs of modes. The notation $\tilde{S}_q/\tilde{D}_p$ denotes the transfer function from forcing electrode $\tilde{D}_p$ to pick-off $\tilde{S}_q$. There is approximately a 10 kHz separation between the $n = 2$ and $n = 3$ modal frequencies and the control architecture discussed in Sec. III effectively prevents interaction between the $n = 2$ and $n = 3$ digital control filters. Thus, each pair of modes can operate as an independent CVG, however, broadband DAC noise is not influenced by the digital filtering and directly drives all modes. For example, the frequency responses from $\tilde{D}_3$ and $\tilde{D}_4$ in Fig. 2 show how $n = 3$ DAC noise can corrupt the $n = 2$ pick-off measurements and for this reason, a pair of high-pass filters are placed after DACs in the D_3 and D_4 channels, and a pair of low-pass are place after the DAC in the D_1 and D_2 channels.

III. Control Architecture

This section describes the filter architecture implemented by the DSP. The $n = 2$ and $n = 3$ control loops are identical in architecture and only differ only in the filter and compensator parameters so the development is described in the context of the $n = 2$ pair. The pair of modes is operated as a force-to-rebalance (FTR) gyro, however, in contrast to previous work by the authors in which the FTR controller was a high-gain phase-shifting filter (eg. [17]), the signal processing is now essentially that of a lock-in amplifier implemented by the DSP (refer to Fig. 4). All signals in Fig. 4 are discrete-time although this is not explicitly noted in the diagram. The demodulation frequency ω_0 is fixed in this implementation (it is not adjusted by a phase-locked loop driving a voltage-controlled oscillator) and is chosen to be near the nominal modal frequency of the $n = 2$ modes, thus, the final transfer function of the lock-in based controller can be mapped to the FTR filter in [17]. This implementation creates a pass-band filter with center frequency at ω_0. The rationale for fixing ω_0 is due to the fact that in this

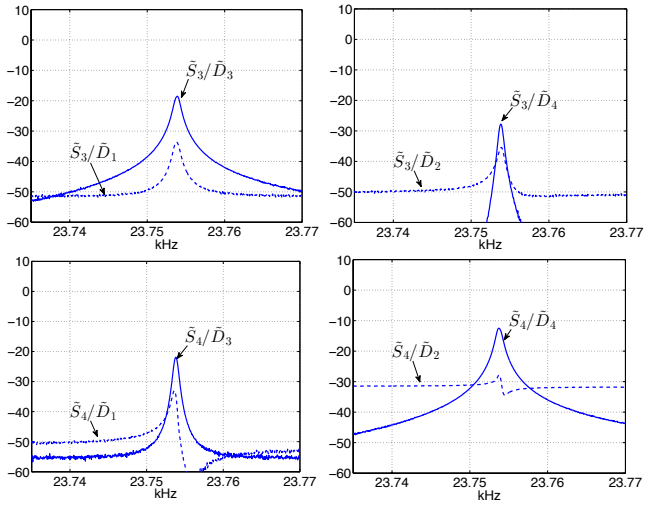

Fig. 3. Frequency responses for electrode arrangement shown in Fig. 1. The solid traces are used for designing the control filters for the $n = 3$ pair, however, the dashed traces show how the forcers for the $n = 2$ pair couple into the $n = 3$ pair.

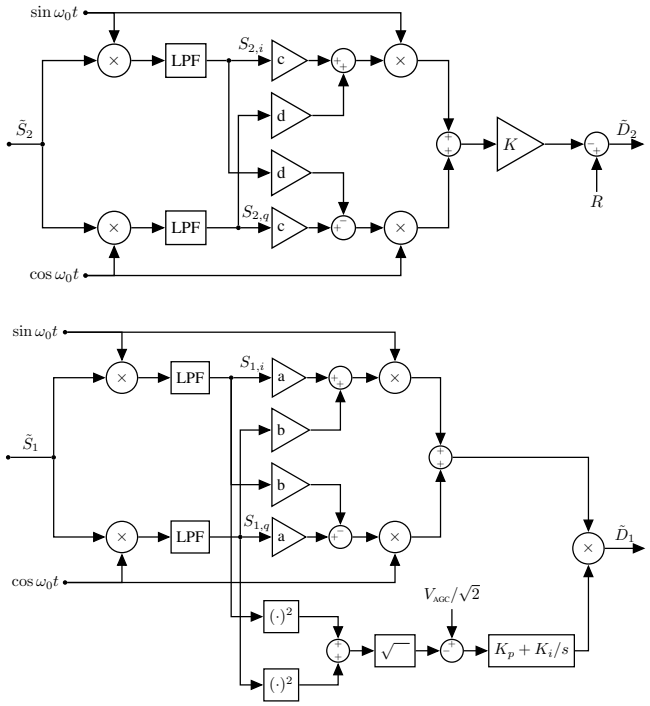

Fig. 4. (Top) Force-to-rebalance controller with lock-in architecture and phase adjustment. (Bottom) Automatic gain control for sensor excitation.

class of resonator there is typically some environmental control so that the gyro operating frequency experiences little drift. The lock-in architecture, however, affords some advantages with regard to adjusting the loop phase. Specifically, the change in the frequency response phase introduced by the analog filtering requires that the phase of the loop must be adjusted by the FTR controller in order to maintain closed-loop stability and minimize peaking in the sensitivity function. Since ω_0 is chosen to be close to the operating frequency, the c and d parameters mix the in-phase and quadrature components of $\tilde{S}_2$, denoted $S_{2,i}$ and $S_{2,q}$, respectively, so that a phase offset is created at the band-pass center frequency ω_0. The phase offset is $-\tan^{-1}(d/c)$. In practice, the parameters c and d are constrained so that $c^2+d^2 = 1$ and are selected so that the sum of the phase offset with the phase of the analog elements (anti-alias and smoothing filters, buffer board dynamics, resonator dynamics) gives the desired loop phase of approximately zero degrees at ω_0 in the negative feedback configuration shown in Fig. 4. The magnitude of the loop transfer function, which determines the gyro bandwidth, is specified with the gain K.

The sensor excitation is achieved with an automatic gain control (AGC) scheme. The AGC can also be implemented using the lock-in architecture as shown in Fig. 4, where the parameters a and b are used to tune the AGC loop phase at ω_0 and also satisfy the constraint $a^2 + b^2 = 1$. The demodulating sinusoids are the same as those used in the FTR loop, i.e. the demodulation frequency is ω_0. Typically, $\{a, b\}$ are different from $\{c, d\}$ because of differences in the phases of the $\tilde{S}_1/\tilde{D}_1$ and $\tilde{S}_2/\tilde{D}_2$ channels. The proportional-integral compensation in the AGC is standard and described elsewhere, eg. [18].

The angular rate and quadrature signals can be extracted by manipulating the baseband signals $S_{1,i}$, $S_{1,q}$, $S_{2,i}$, and $S_{2,q}$. For the analysis it can be assumed that the AGC establishes a constant amplitude sinusoidal response for $\tilde{S}_1$ and that the rate and quadrature signals can be modeled as disturbances reflected to the output of the FTR controller as shown in Fig. 4.

Thus, we assume $\tilde{S}_1 = V_{\text{AGC}} \sin(\omega_n t + \phi_A)$, where V_{AGC} is the amplitude of the steady-state pickoff voltage established by the AGC loop, ϕ_A is the phase of the response and ω_n is the operating frequency of the gyro. Note that ω_n is close to, but generally not equal to, the demodulation frequency ω_0, thus, the frequency offset parameter δ_ω is defined such that $\omega_n = \omega_0 + \delta_\omega$. The baseband components in the AGC are given by

$$\begin{aligned} S_{1,i} &= \frac{V_{\text{AGC}}}{2}\cos(\delta_\omega t)\cos\phi_A - \frac{V_{\text{AGC}}}{2}\sin(\delta_\omega t)\sin\phi_A, \\ S_{1,q} &= \frac{V_{\text{AGC}}}{2}\sin(\delta_\omega t)\cos\phi_A - \frac{V_{\text{AGC}}}{2}\cos(\delta_\omega t)\sin\phi_A, \end{aligned} \tag{1}$$

where it has been assumed that the low-pass filters, shown as the LPF blocks in Fig. 4, pass only the baseband signals.

The signal introduced into the FTR loop by an angular rate of rotation Ω and quadrature Q can be modeled as a disturbance, denoted R, located at the output of the FTR controller

$$R(t) = \gamma\Omega\cos(\omega_n t + \phi_r) + \gamma Q \sin(\omega_n t + \phi_r),$$

where γ captures the degree of Coriolis coupling between the modes and the fact that the disturbance, which can be fundamentally understood as forces on the resonator, have been expressed in terms of an equivalent voltage. Note that the disturbance appears at the gyro operating frequency ω_n, and it also has an associated phase ϕ_r. In a high-gain FTR loop, it can be assumed that the controller voltage issuing from the K gain block completely cancels the Coriolis and quadrature induced disturbance. In other words, the output of the K gain

block is also R. Thus, it is possible to compute the baseband signals in the FTR controller which produce this signal,

$$\begin{bmatrix} -\sin(\delta_\omega t) & -\cos(\delta_\omega t) \\ \cos(\delta_\omega t) & -\sin(\delta_\omega t) \end{bmatrix} \begin{bmatrix} \cos\phi_r & \sin\phi_r \\ \sin\phi_r & -\cos\phi_r \end{bmatrix} \begin{bmatrix} \Omega \\ Q \end{bmatrix} = \frac{K}{\gamma} \begin{bmatrix} c & d \\ -d & c \end{bmatrix} \begin{bmatrix} S_{2,i} \\ S_{2,q} \end{bmatrix} \tag{2}$$

The slowly varying components at frequency δ_ω can be eliminated by substituting (1) into (2) and solving for Ω and Q,

$$\begin{aligned} \begin{bmatrix} \Omega \\ Q \end{bmatrix} &= \frac{2K}{V_{\text{AGC}}\gamma} \begin{bmatrix} -\cos\phi_r & -\sin\phi_r \\ -\sin\phi_r & \cos\phi_r \end{bmatrix} \begin{bmatrix} -\sin\phi_A & \cos\phi_A \\ \cos\phi_A & \sin\phi_A \end{bmatrix} \\ &\quad \times \begin{bmatrix} c & -d \\ d & c \end{bmatrix} \begin{bmatrix} S_{1,i} & S_{1,q} \\ S_{1,q} & -S_{1,i} \end{bmatrix} \begin{bmatrix} S_{2,i} \\ S_{2,q} \end{bmatrix} \\ &= \frac{2K}{V_{\text{AGC}}\gamma} \begin{bmatrix} \cos\theta & \sin\theta \\ -\sin\theta & \cos\theta \end{bmatrix} \begin{bmatrix} S_{1,i} & S_{1,q} \\ S_{1,q} & -S_{1,i} \end{bmatrix} \begin{bmatrix} S_{2,i} \\ S_{2,q} \end{bmatrix}. \end{aligned} \tag{3}$$

Note that there is a product of three orthogonal matrices in (3) which can be represented as a single orthogonal matrix parameterized by angle θ as shown. Although, ϕ_A and ϕ_r can be measured, it is not necessary to do so because θ can be determined from a calibration experiment: a known angular rate profile is applied to the sensor, the baseband signals are mixed according to (3) and then θ is selected so that the derived signal Q is uncorrelated with the known angular rate. This also demonstrates that γ and V_{AGC} need not be explicitly determined (although the latter is known since is the reference amplitude for the PI compensation in the AGC) because the scaling $2K/V_{\text{AGC}}\gamma$ can also be determined from the calibration experiment.

IV. Single- and dual-pair gyro operation

A. Test environment and scale factor measurement

The unpackaged resonator and buffer board reside in a vacuum chamber with additional electronics located outside the chamber, thus, rigorous environmental testing of the sensor is not possible and must be postponed until hermetically packaged resonators with compact buffer and control electronics become available. Therefore, the objective of the experiments is to demonstrate proofs-of-concept. Nevertheless, the resonator temperature is unregulated so thermal transients are experienced over the course of an experiment, albeit with a range limited to a few degrees Celsius. The vacuum chamber pressure is also allowed to reach $100\,\mu$Torr before commencing an experiment, however, because the ultimate vacuum is $10\,\mu$Torr, all experiments can be assumed to have a vacuum level in the range 10-100 μTorr. Thus, the effects of vacuum and temperature transients are present in the data, however, they are not quantified or used for compensation in this paper.

The absence of environmental control, even in benign laboratory conditions, exposes the resonator to enough of a changing environment to induce significant drift in the angular rate offsets derived from the $n = 2$ pair and $n = 3$ pair. It will be shown that the drifting offsets are correlated when both pairs modes are simultaneously operating in the resonator, a configuration that is designated "dual-pair" operation. Thus, the long-term drift in the offsets can be used to calibrate each other to improve the overall stability of the "fused" angular rate signal, i.e. the rate signal derived from processing both basic angular rate measurements into a single signal.

The vacuum chamber is equipped with a rotary feedthrough for scale factor estimation. It is necessary to estimate the scale factors associated with the $n = 2$ and $n = 3$ modal pairs so that the pick-off voltage noise spectrum can be converted into an equivalent rate noise spectrum. Measurement of the scale factors is accomplished using the rotary vacuum feedthrough to turn the resonator through a known angle. The subsequent response of the voltage signals proportional to Ω and Q in (3) are integrated over the duration of the calibration experiment, yielding quantities whose units are V-s. The known angle, expressed in degrees, is normalized by the integrated voltages so scale factors are estimated with units of $(^\circ/\text{s})/\text{V}$. With this definition, a lower scale factor indicates higher sensitivity. This technique is suitable for estimating nominal scale factors, however, it cannot be used to determine scale factor stability.

B. Single-pair baseline performance

The controller and filtering parameters are listed in Table II for both pairs of modes. These controller parameters remain the same for single- or dual-pair operation –it is simple a matter of closing the relevant loops in order to operate the pair(s) of interest. The angular rate extracted from $n = 2$ pair is denoted Ω_2 and the angular rate extracted from the $n = 3$ pair is denoted Ω_3. The scale factors, defined $\mathbf{SF} = 2K/V_{\text{AGC}}\gamma$, and bandwidths (denoted BW) associated with each rate measurement are listed in Table III. As shown in this table, the scale factor for the $n = 2$ pair of modes is roughly one sixth of that of the $n = 3$ pair of modes. This difference is primarily attributed to the difference in AGC channel displacement associated with each pair of modes. The AGC displacement is given by $V_{\text{AGC}}/\omega_n K_c K_T$, where K_c is the transduction gain of the capacitive pick off electrodes, which can be calculated from the capacitance model of the resonator-electrode geometry, and V_{AGC} is the amplitude of the sinusoidal voltage representing the AGC pick-off (this is the reference amplitude in the AGC loop in Fig. 4). The transresistance gain of the buffer electronics is 10^7 Ohm for both pairs of modes, however, the $n = 3$ pair has an additional gain of 5 in the AGC signal path, thus, $K_T = 10^7$ Ohm for the $n = 2$ AGC channel, and $K_T = 5 \times 10^7$ Ohm for the $n = 3$ AGC channel. The resonator transduction parameters are also summarized in Table II. As indicated in the table, the modal displacement amplitude of the $n = 2$ mode is more than an order of magnitude larger than that of the $n = 3$ mode, despite the fact that the modes are driven by excitation sinusoids with approximately the same amplitudes. This difference in modal displacement can be attributed to a number of factors. For example, ratio of the modal stiffness to modal mass is higher for the $n = 3$ pair mode and the $n = 3$ quality factors are lower than their $n = 2$ counterparts. Thus, for a given input force, the displacement produced by the $n = 3$ modes is inherently smaller.

TABLE II
SUMMARY OF CONTROL FILTER AND TRANSDUCTION PARAMETERS

Parameter	$n = 2$ pair	$n = 3$ pair
ω_0 (kHz)	13.520	23.750
V_{AGC} (V)	1.0	0.5
LPF	4-pole, 100 Hz	4-pole, 100 Hz
K	44	95
AGC disp. (μm)	0.7	0.06
K_c (μA/m/s)	1.69	1.12

TABLE III
SINGLE- VS. DUAL-PAIR GYRO PERFORMANCE

Configuration	**SF** ((∘/s)/V)	BW (Hz)	ARW (∘/$\sqrt{\text{hr}}$)
$n = 2$, single	-19.9	10	0.025
$n = 2$, dual	-20.2	10	0.031
$n = 3$, single	131	25	0.52
$n = 3$, dual	133	25	0.78

With the identified scale factors in hand, the statistics of the noise and offset associated with Ω_2 are first quantified when the $n = 3$ pair is uncontrolled ($\tilde{D}_1$ and $\tilde{D}_1$ are grounded). Then, the noise statistics of Ω_3 are quantified when the $n = 2$ pair is uncontrolled ($\tilde{D}_3$ and $\tilde{D}_4$ are grounded). The Allan deviation and power spectral densities of the single-pair angular rates are shown in Figs. 5 and 6, respectively. No compensation strategies, such as temperature- or frequency-based compensation or quadrature control, were employed for mitigating rate offset drift. The angle random walk (ARW) can be estimated from the low frequency asymptote in the spectral density graphs but is more difficult to discern from the Allan deviation charts. The ARW figures for single-pair operation are also reported in Table III.

The noise spectra in Fig. 6 exhibit the typical sigmoid shape with high-Q, mode-matched resonators [14], however, the total noise powers associated with Ω_2 and Ω_3 are quite different. As

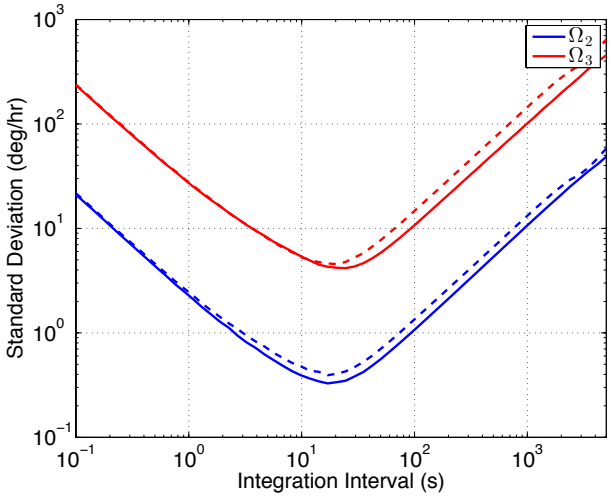

Fig. 5. Allan deviation of Ω_2 and Ω_3 associated with single-pair (solid) and dual-pair (dash) operation.

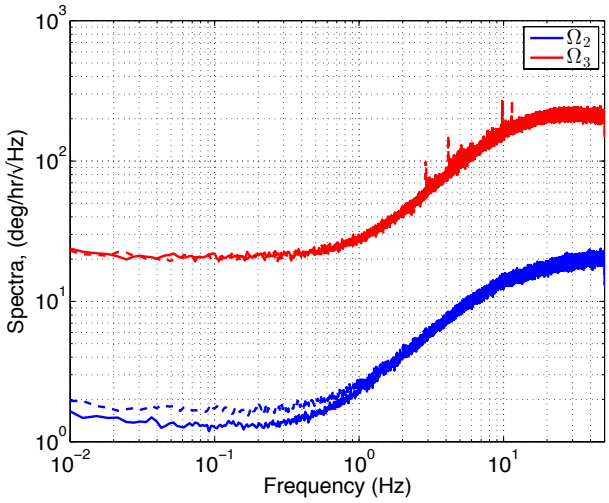

Fig. 6. Spectral densities of Ω_2 and Ω_3 associated with single-pair (solid) and dual-pair (dash) operation.

mentioned above, this is due to the different scale factors, but also because the pick-off voltage noise spectrum is slightly higher at the $n = 3$ frequency ($37.5\mu\text{V}/\sqrt{\text{Hz}}$ for $n = 2$ versus $52.5\mu\text{V}/\sqrt{\text{Hz}}$ for $n = 3$). The low-frequency knee in the spectral densities is located at approximately 1 HZ for Ω_3 versus 0.5 Hz for Ω_2. This is attributed to the lower quality factor of the $n = 3$ modes.

C. Dual-pair performance

This section demonstrates that both pairs can be operated simultaneously, thereby providing two angular rate measurements from one resonator. The key ingredients are already in place. The isolation of a given pair of modes from the other pair due to the lock-in architecture implies that both pairs can be operated simultaneously without risk of destabilization. Furthermore, broadband disturbances created by the DAC noise are diminished by appropriate analog filtering. The noise spectra of Ω_2 and Ω_3 obtained from simultaneous operation essentially achieves the performance corresponding single-pair operation –only slight degradation in performance is measured as shown in Figs. 5 and 6 and Table III. The marginal increase in the Ω_2 ARW is attributed to the $n = 3$ DAC noise which is not completely eliminated by the analog filters.

Time domain angular rate measurements are shown in Fig. 7 when the rotary feedthrough is turned through 90 degrees. This figure clearly demonstrates that the sensor yields two simultaneous estimates of angular rate. Also of interest are the long-term drifts in the rate offsets when the sensor is not rotating. The offset drifts can be viewed by filtering the Ω_2 and Ω_3 signals through a moving average filter whose averaging interval is approximately equal to the integration time at which the Allan deviation is minimum. The low-pass filtered signals are denoted $\Omega_{2,lp}$ and $\Omega_{3,lp}$. For example, a 10-second moving average yields the Ω_2 and Ω_3 offsets shown in Fig. 8 for five experiments ranging in duration of 6 hours to over 15 hours. It is clear that for a given experiment the Ω_2 and Ω_3 offsets are strongly correlated, however, the offsets appear uncorrelated

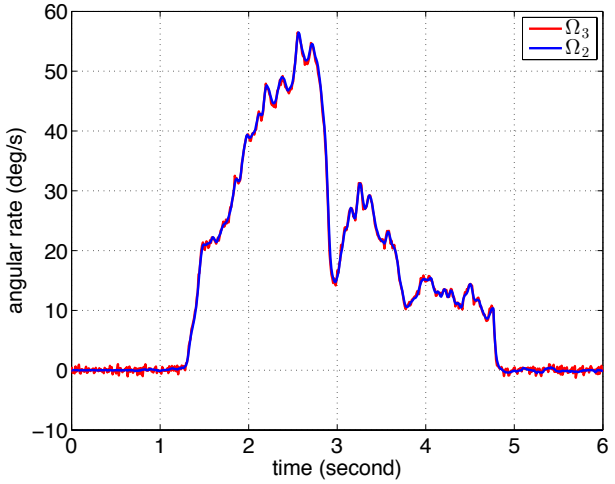

Fig. 7. Simultaneous angular rate measurements from a scale factor calibration test.

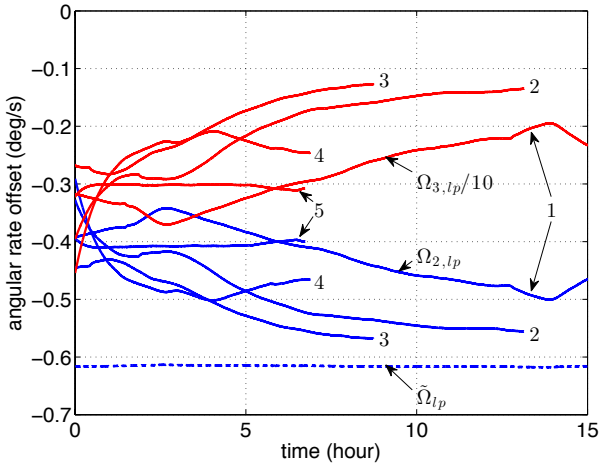

Fig. 8. Low-pass filtered signals $\Omega_{2,lp}$ (blue, solid) and $\Omega_{3,lp}/10$ (red) from five dual-pair experiments (labeled "1" through "5") exhibit strong correlation within a given experiment. The derived rate $\tilde{\Omega}_{lp} = \lambda\Omega_{2,lp} + (1-\lambda)\Omega_{3,lp}$ (blue, dash) is shown from experiment 1, where $\lambda = 0.9192$.

from one experiment to the next. In fact, if the rate signals for the 15 hour experiment are combined to create the signal $\tilde{\Omega}_{lp} := \lambda\Omega_{2,lp} + (1-\lambda)\Omega_{3,lp}$, where $\lambda = 0.9192$, then the offset drift of $\tilde{\Omega}_{lp}$ is drastically reduced as shown in Fig. 8. This motivates the search for a filter structure that combines both rate measurements into a low noise rate estimate with reduced offset drift. This is the subject of the next section.

V. Filter Architecture for Fusion of Rate Signals

The fact that the long-term drift in the Ω_2 and Ω_3 offsets are strongly correlated and can be combined into a signal with lower drift suggests that it should be possible to combine Ω_2 and Ω_3 into a single estimate of the angular rate that also retains the benefits of the lower noise associated with Ω_2 at shorter integration times. For example, simply combining the rates into the signal $\tilde{\Omega} = \lambda\Omega_2 + (1-\lambda)\Omega_3$ will produce a rate

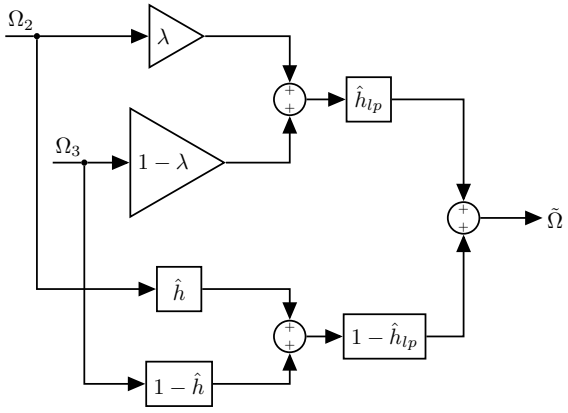

Fig. 9. Filter structure for fusing Ω_2 and Ω_3 into a single signal. The filter blocks are specified in transfer function form.

estimate with reduced offset drift, however, at short integration times the Allan variance of this signal is approximately

$$\sigma^2_{AV}(\tilde{\Omega}) \approx \lambda^2\sigma^2_{AV}(\Omega_2) + (1-\lambda)^2\sigma^2_{AV}(\Omega_3),$$

where $\sigma^2_{AV}(\Omega_2)$ and $\sigma^2_{AV}(\Omega_3)$ are the Allan variances of Ω_2 and Ω_3, respectively. The large noise power in Ω_3 relative to Ω_2 produces $\sigma^2_{AV}(\tilde{\Omega}) > \sigma^2_{AV}(\Omega_2)$ at short integration times, which is undesirable. This is overcome by implementing the filter structure shown in Fig. 9. As described above, λ is a parameter that is related to the long-term correlation of Ω_2 and Ω_3, h_{lp} denotes the impulse response of a low-pass moving average filter (the transfer function is denoted $\hat{h}_{lp}$), and h is the impulse response of a second filter (transfer function $\hat{h}$) that is designed to reduce the variance of $\tilde{\Omega}$ at shorter integration intervals. The process for designing λ, h_{lp} and h is described in the Appendix.

It is clear from Fig. 8 that the offset variation does not repeat from experiment-to-experiment, however, the filter architecture in Fig. 9 can be applied to dual-pair rates from the five experiments in which the filters are populated by analyzing the data from a single experiment. For example, assuming h_{lp} is a 10 second moving average low-pass filter –refer to (4)– λ and h can be generated using the Ω_2 and Ω_3 data from the experiment labeled "1" in Fig. 8. This yields $\lambda = 0.9192$ and h whose impulse response is shown in Fig. 11. Note that h is very close to a unit impulse because the noise power in $\Omega_{3,hp}$ is much larger than the noise power in $\Omega_{2,hp}$ (the subscript notation is described in the Appendix). These filters are fixed and then applied to the remaining dual-pair test data. The Allan deviation of $\tilde{\Omega}$ derived from each dual-pair experiment is shown in Fig. 10. There is significant improvement in long-term bias stability with short-term noise essentially equal to that of Ω_2. In fact, the stability of $\tilde{\Omega}$ has improved to the point where the ARW trend is readily identifiable in the Allan deviation, whereas it is obscured in the single-pair Allan deviation. The fused rate signal has an ARW figure of $0.027^\circ/\sqrt{\text{hr}}$. The angle white noise (AWN) asymptote is also shown in Fig. 10.

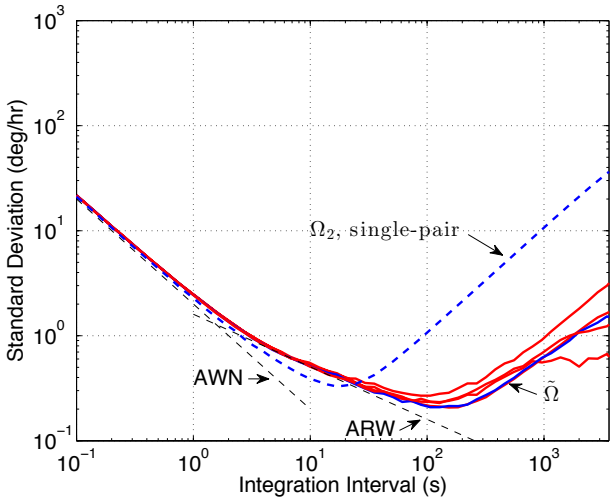

Fig. 10. Allan deviation of $\tilde{\Omega}$ across multiple data runs. The solid blue trace was used to fit the filters for the fusion of Ω_2 and Ω_3 into $\tilde{\Omega}$. For comparison, the blue dash is the Allan deviation for Ω_2 from a single-pair experiment. The angle white noise (AWN) and angle random walk (ARW) asymptotes for $\tilde{\Omega}$ are also shown.

VI. Conclusion

An axisymmetric resonator has been modified so that the $n = 2$ elliptical pair of modes and the $n = 3$ pair of modes are both degenerate. The angular rate extracted from the $n = 2$ pair is contrasted to that of the $n = 3$ pair. Although the $n = 3$ pair exhibits higher noise, the offsets are correlated when both pairs are simultaneously operated as CVGs. The correlation of the offsets allows the fusing of the two angular rate measurements into a single rate estimate with improved long-term stability and low short-term noise. In fact, the integration interval over which the Allan deviation is less than $1\,^\circ$/hr was extend from 100 seconds to a minimum of 1000 seconds for the fused angular rate signal, thus, this is a complementary technique for compensating offset drift and can be used in conjunction with other environmental control and self-calibration strategies. It is also possible to configure each rate measurement for different sensing objectives. For example, the $n = 2$ pair can be configured as a high-sensitivity, low-dynamic range measurement whereas the $n = 3$ pair can be configured for higher bandwidth and dynamic range.

The results can be improved by considering modifications to the present resonator design. Whether one pair or both pairs of modes are used for sensing, the design suffers from relatively small electrode area compared to internal electrode design, eg. [4]. The addition of internal electrodes arranged for differential sensing and forcing, instead of just the external perimeter electrodes in an unbalanced arrangement, can significantly boost the electrode area, which will produce a concomitant reduction in ARW. The internal electrodes would also facilitate manipulating the modal frequencies by mass perturbation since certain harmonics that are important in the modes shapes are only prominent for the interior rings, eg. [16].

The proposed control technique is analogous to a lock-in amplifier applied to all measurement channels followed by filtering and then remodulation of baseband signals to produce the forcing signals. This approach achieves not only exceptional isolation of each pair of modes and eliminates interaction between the various channels but it also allows facile adjustment of the loop phases, which is important for achieving the best possible stability margins. One issue which is not associated with the control technique but rather the use of DACs, is the broadband noise created by the DACs –the noise from the $n = 3$ DACs can disturb the $n = 2$ pair leading to increased angle random walk associated with Ω_2. Thus, analog filters are still required to remove these disturbances, however, differential forcing with an expanded set of electrodes would also mitigate the DAC disturbances introduced across the pairs of modes.

Appendix
Derivation of filters for fusing rate signals

The filter structure for blending the two rate measurements is shown in Fig. 9. It is assumed that angular rate estimates Ω_2 and Ω_3 are produced with the same bandwidth. If this is not the case, then the high bandwidth measurement can be filtered so that its bandwidth is constrained to be equal to the other measurement or, alternatively, the filter structure can be modified to accommodate the different bandwidth signals. The first requirement is that the scalar transfer functions in Fig. 9 sum to one

$$\tilde{\Omega}/\Omega_2 + \tilde{\Omega}/\Omega_3 = 1,$$

where $\tilde{\Omega}/\Omega_2$ denotes the transfer function from Ω_2 to $\tilde{\Omega}$ and so forth. This ensures in the noise free case that $\tilde{\Omega} = \Omega_2 = \Omega_3$. This constrains the filter structure to that of a complementary filter (eg. [19]) and it can be verified that the structure in Fig. 9 satisfies this criterion. The discrete-time data from zero-rate input dual-pair "drift" tests are used in these calculations. It is assumed that the data are associated with sample period t_s ($t_s = 0.01$ second for the data reported in this paper). The steps for determining h_{lp}, λ, and h are as follows:

1) h_{lp} is a moving average filter of length N and with impulse response

$$h_{lp}[k] = \begin{cases} \frac{1}{N} & k \in [0, N-1] \\ 0 & \text{otherwise} \end{cases}, \qquad (4)$$

where k denotes the sample index. The averaging time $T = Nt_s$ is chosen so that when this filter is applied to Ω_2 and Ω_3, the short-term noise is eliminated and the long-term correlation between the filtered signals is revealed. The filtered signals are denoted $\Omega_{2,lp}$ and $\Omega_{3,lp}$, where $\Omega_{2,lp} = h_{lp} * \Omega_2$ and $\Omega_{3,lp} = h_{lp} * \Omega_3$, and where $*$ denotes convolution.

2) The parameter λ is chosen so that the long-term drift of $\lambda\Omega_{2,lp} + (1-\lambda)\Omega_{3,lp}$ is minimized. It is determined from a simple least-squares criterion

$$\min_{\lambda,c} \sum_{k=0}^{M-1} \left(\lambda\Omega_{2,lp}[k] + (1-\lambda)\Omega_{3,lp}[k] + c\right)^2, \qquad (5)$$

where c is a parameter that accounts for any residual rate offset and where the data set is M samples in length and

starts with index $k = 0$. It is assumed $M >> N$ so that the smoothed data is used in the minimization (5) and that the filter transients can be removed.

3) The filter h is determined so that variance of the signal e in the block diagram below is minimized,

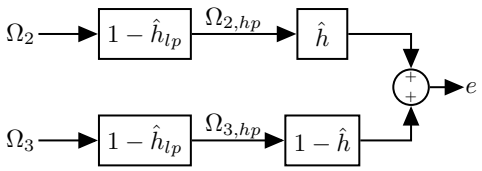

This diagram is functionally identical to the lower section in Fig. 9, however, it shows how h is computed: the rate measurements are high-pass filtered, i.e. $(\delta - h_{lp}) * \Omega_2$ and $(\delta - h_{lp}) * \Omega_3$, to produce the signals $\Omega_{2,hp}$ and $\Omega_{3,hp}$; h is designed so that the variance of $e = h * \Omega_{2,hp} + (\delta - h) * \Omega_{3,hp}$ is minimized. In this time-domain description, δ represents the discrete-time unit pulse function.

The filter h can be determined once the auto- and cross-correlations of $\Omega_{2,hp}$ and $\Omega_{3,hp}$, are known. The cross-correlation of $\Omega_{2,hp}$ and $\Omega_{3,hp}$, the auto-correlation of $\Omega_{2,hp}$ and the auto-correlation of $\Omega_{3,hp}$ are denoted R_{23}, R_{22} and R_{33}, respectively. It can be assumed that h is a finite-impulse response filter. Let $\vec{h} = \left[h[0], h[1], \cdots, h[m-1]\right]^T$, i.e. a vector containing the m impulse response samples of the filter. Then, the filter that minimizes the mean-square value of e is determined from

$$P\vec{h} = \vec{q}, \tag{6}$$

where the positive definite $m \times m$ matrix P, and m-element vector $\vec{q}$, are formed from the correlation samples. It can be shown that for this specific filtering problem the (i, j) entry of P, denoted $P_{i,j}$, $i, j = 1, \ldots, m$, and the ith entry of $\vec{q}$, denoted $\vec{q}_i$, are given by

$$\begin{aligned} P_{i,j} &= R_{22}[i-j] + R_{33}[i-j] - R_{32}[i-j] - R_{23}[i-j] \\ \vec{q}_i &= R_{33}[i] - R_{23}[i], \end{aligned} \tag{7}$$

where $R_{22}[l]$ represents the lth sample of the signal R_{22} and so forth. Since $R_{23}[i] = -R_{32}[-i]$, the cross-correlations need only be computed for non-negative indices.

The computations in Steps 1, 2, and 3 are performed with angular rate data from experiment "1," whose offsets are shown in Fig. 8. First, λ is computed to be 0.9192 when $N = 1000$ (corresponding to an averaging window of 10 seconds). The correlation functions for $\Omega_{2,hp}$ and $\Omega_{3,hp}$ are shown in Fig. 11. The filter h is then computed using (6) and (7) and is also shown in Fig. 11. The optimal filter for this data is very nearly a unit impulse because the noise power in $\Omega_{3,hp}$ is much larger than the power in $\Omega_{2,hp}$ (evident in the autocorrelations where $R_{22}[0] < R_{33}[0]/100$). Thus, $\Omega_{3,hp}$ is deemphasized for this sensor when computing the short-term angular rate. In general, a standard Wiener filter problem cannot be formulated because the spectral density of the angular rate is not known. Thus, this approach, in the most ideal scenario in which the spectral densities of $\Omega_{2,hp}$ and $\Omega_{3,hp}$ are equal, will only yield a reduction of

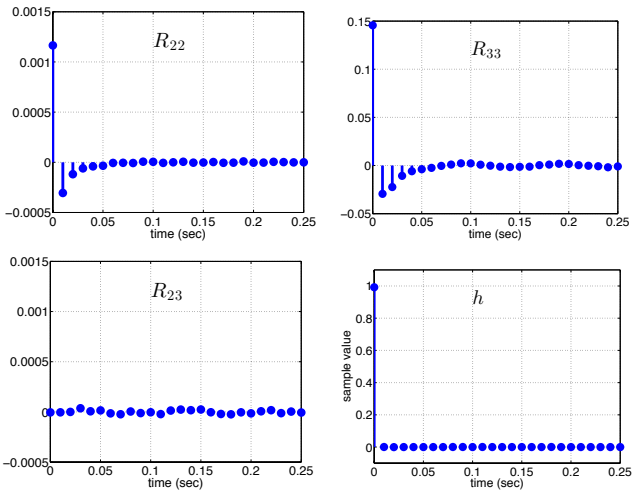

Fig. 11. Correlations functions R_{22}, R_{23}, and R_{33}, and the impulse response of filter h.

0.5 in the short-term noise power in the combined signal $\tilde{\Omega}$. Nevertheless, the filter architecture in Fig. 9 and the steps outlined in this appendix provide a sensible and systematic approach to providing a fused angular rate estimate using Ω_2 and Ω_3 with reduced offset drift and short-term noise that does not exceed that of the lowest noise measurement during dual-pair operation.

REFERENCES

[1] G. He and K. Najafi, "A single-crystal silicon vibrating ring gyroscope," in *Technical Digest. MEMS 2002 IEEE International Conference. Fifteenth IEEE International Conference on Micro Electro Mechanical Systems (Cat. No.02CH37266)*, Jan 2002, pp. 718–721.

[2] S. Nitzan, C. Ahn, T.-H. Su, M. Li, E. Ng, S. Wang, Z. Yang, G. O'Brien, B. Boser, T. Kenny, and D. Horsley, "Epitaxially-encapsulated polysilicon disk resonator gyroscope," in *Proc. IEEE MEMS*, Taipei, Jan. 2013, pp. 625–628.

[3] T. H. Su, S. H. Nitzan, P. Taheri-Tehrani, M. H. Kline, B. E. Boser, and D. A. Horsley, "Silicon mems disk resonator gyroscope with an integrated cmos analog front-end," *IEEE Sensors Journal*, vol. 14, no. 10, pp. 3426–3432, Oct 2014.

[4] A. Challoner, H. Ge, and J. Liu, "Boeing disc resonator gyroscope," in *Proc. 2014 IEEE/ION Position, Location and Navigation Symp.*, Monterey, CA, May 2014, pp. 504–514.

[5] C. H. Ahn, E. J. Ng, V. A. Hong, J. Huynh, S. Wang, and T. W. Kenny, "Characterization of oxide-coated polysilicon disk resonator gyroscope within a wafer-scale encapsulation process," *Journal of Microelectromechanical Systems*, vol. 24, no. 6, pp. 1687–1694, Dec 2015.

[6] I. P. Prikhodko, S. A. Zotov, A. A. Trusov, and A. M. Shkel, "What is MEMS gyrocompassing? comparative analysis of maytagging and carouseling," *Journal of Microelectromechanical Systems*, vol. 22, no. 6, pp. 1257–1266, 2013.

[7] E. Tatar, T. Mukherjee, and G. K. Fedder, "Stress effects and compensation of bias drift in a MEMS vibratory-rate gyroscope," *Journal of Microelectromechanical Systems*, pp. 1–11, 2017, to appear.

[8] M. Kline, Y.-C. Yeh, B. Eminoglu, I. Izyumin, M. Daneman, D. Horsley, and B. Boser, "MEMS gyroscope bias drift cancellation using continuous-time mode reversal," in *Solid-State Sensors, Actuators and Microsystems (TRANSDUCERS & EUROSENSORS XXVII), 2013 Transducers & Eurosensors XXVII: The 17th International Conference on*. IEEE, 2013, pp. 1855–1858.

[9] A. A. Trusov, M. R. Phillips, G. H. McCammon, D. M. Rozelle, and A. D. Meyer, "Continuously self-calibrating CVG system using hemispherical resonator gyroscopes," in *Inertial Sensors and Systems (ISISS), 2015 IEEE International Symposium on*, Hapuna Beach, Hawaii, March 2015, pp. 1–4.

[10] P. Taheri-Tehrani, A. D. Challoner, O. Izyumin, B. Boser, and D. Horsley, "A new electronic feedback compensation method for rate integrating gyroscopes," in *Inertial Sensors and Systems, 2016 IEEE International Symposium on*. IEEE, 2016, pp. 9–12.

[11] G. Bryan, "On the beats in the vibrations of a revolving cylinder or bell," in *Proc. Cambridge Philosophical Society*, vol. VII, Nov. 1890, pp. 101–111.

[12] D. Schwartz, D. Kim, P. Stupar, J. DeNatale, and R. M'Closkey, "Modal parameter tuning of an axisymmetric resonator via mass perturbation," *J. Microelectromech. Syst.*, vol. 24, no. 3, pp. 545–555, June 2015.

[13] S. Wong, C. Fox, and S. McWilliam, "Thermoelastic damping of the in-plane vibration of thin silicon rings," *Journal of Sound and Vibration*, vol. 293, no. 1??2, pp. 266 – 285, 2006.

[14] D. Kim and R. M'Closkey, "Spectral analysis of vibratory gyro noise," *IEEE Sensors J.*, vol. 13, pp. 4361–4374, Nov. 2013.

[15] H. Ge, D. Kim, and R. M'Closkey, "Simultaneous exploitation of the fundamental and higher order wineglass modes in a vibratory gyro," in *Inertial Sensors and Systems (ISISS), 2015 IEEE International Symposium on*, Hapuna Beach, Hawaii, March 2015, pp. 1–4.

[16] A. H. Behbahani, D. Kim, P. Stupar, J. DeNatale, and R. T. M'Closkey, "Tailored etch profiles for wafer-level frequency tuning of axisymmetric resonators," *J. Microelectromech. Syst.*, pp. 1–11, 2017, to appear.

[17] Y.-C. Chen, R. T. M'Closkey, T. A. Tran, and B. Blaes, "A control and signal processing integrated circuit for the jpl-boeing micromachined gyroscopes," *IEEE Trans. Contr. Syst. Technol.*, vol. 13, no. 2, pp. 286–300, March 2005.

[18] R. T. M'Closkey, A. Vakakis, and R. Gutierrez, "Mode localization induced by a nonlinear control loop," *Nonlinear Dynamics*, vol. 25, pp. 221–236, 2001.

[19] B. Buttkus, *Spectral Analysis and Filter Theory in Applied Geophysics*. Springer-Verlag, 2000.